

The role of superradiance in cosmic fast radio bursts

Abhilash Mathews

Supervisor: Prof. Martin Houde

Department of Physics & Astronomy

The University of Western Ontario

Honours Thesis

Abstract

A fast radio burst (FRB) was first reportedly detected in 2001 as a flare lasting a few milliseconds with a peak flux density of 30 ± 10 Jansky (Jy). In following years, FRBs have been more widely observed but their origins are still without adequate explanation. Recent work suggests astrophysical sources (e.g. molecular clouds, circumstellar envelopes) exhibit the necessary conditions for superradiance, and we consider this phenomenon as a possible mechanism to explain the emergence of FRBs. Superradiance involves a quantum mechanically coupled system coherently radiating to produce photon emissions stronger than an analogous system with matching dimensions and molecular density but independently radiating molecules instead. Using the Heisenberg representation of quantum mechanics to analyze superradiance, this project aims to develop a numerical code to simulate the time and spatial evolution of propagating electromagnetic fields in environments FRBs are suspected to occur. With this we will investigate whether superradiance is a suitable model to describe cosmic FRBs.

Introduction

In 1954 R. H. Dicke pioneered superradiance, which describes the phenomenon where N sufficiently close molecules interact with a common electromagnetic field to radiate coherently. By modelling the system as one composed of N identical spin- $\frac{1}{2}$ particles, Dicke's formalism predicts bursts of anisotropic radiation where an electromagnetic pulse propagates through an inverted sample, with a superradiance characteristic timescale, T_R , approximately N times shorter than the natural lifetime of the excited state, τ_{sp} (defined as the inverse of the Einstein A coefficient) [Dicke, 1954]. Superradiance is described as a collective and coherent radiation phenomenon because when considering a completely inverted sample with length smaller than the wavelength of radiation, λ , a photon emitted by a molecule will arrive at a neighbouring molecule with definite relative phase. This initial photon can induce the neighbouring molecule in the sample volume, V , to emit another photon with the same mode, phase, and direction. Continuing this process throughout the entire sample of identical molecules results in a photon cascade producing directed photon emissions as demonstrated in Figure 1. This is contrary to the isotropic and exponentially decaying nature typical of non-coherent radiation processes. Based solely on spontaneous decay, radiation from a sample of N molecules would have an intensity directly proportional to N . But a defining feature of superradiance is that an ensemble of N molecules behave as a single quantum mechanical system with a pulsed intensity, I_{SR} , now linearly proportional to N^2 . For lengths larger than λ , if the incoming and radiated photons do not have equivalent directions, coherence in the medium diminishes since only local groups of molecules are similar in phase, which weakens the radiative coupling of the entire system [Rajabi and Houde, 2016a].

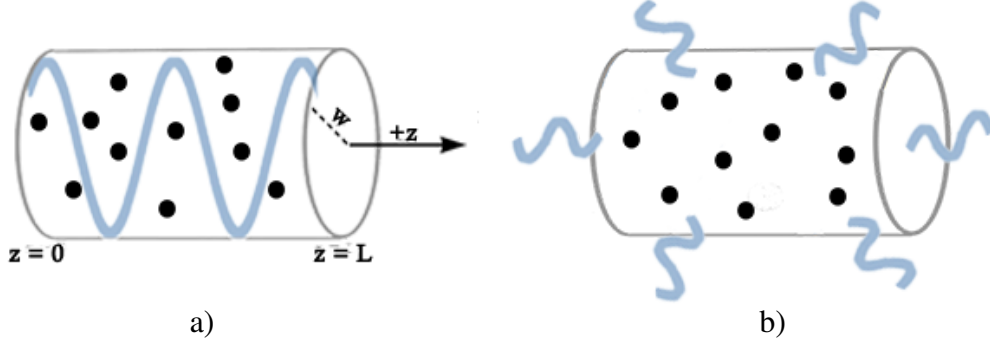


Figure 1. Two samples of inverted molecules with cylindrical geometry exhibiting (a) superradiance and (b) ordinary fluorescence. A radiation field propagates through the initially inverted medium with small beaming angle primarily along the z -axis in the superradiant case.

To expand on the theory of superradiance, we consider a quantum electrodynamical approach to describe radiation interactions with a molecular sample. Instead of using the Schrödinger representation and assessing a density matrix of dimensions $N \times N$, the following analysis utilizes the Heisenberg picture. This approach is economical when modelling numerous molecules because one only needs to evaluate the time evolution of the relevant field and molecular observables. Postulating a Hamiltonian which includes the energy of the inverted molecules, free radiation field, and field-molecule interactions in the electric dipole approximation gives

$$\hat{H} = \hat{H}_{\text{mol}} + \hat{H}_{\text{rad}} + \hat{H}_{\text{int}} \quad (1)$$

$$\hat{H}_{\text{mol}} = \hbar\omega_0 \sum_{i=1}^N \hat{R}_3^{(i)} \quad (2)$$

$$\hat{H}_{\text{rad}} = \sum_{\mathbf{k}, \zeta} \hbar\omega_k (\hat{a}_{\mathbf{k}, \zeta}^\dagger \hat{a}_{\mathbf{k}, \zeta} + \frac{1}{2}) \quad (3)$$

$$\hat{H}_{\text{int}} = - \sum_{i=1}^N \mathbf{d}^{(i)} \cdot (\hat{R}_+^{(i)} + \hat{R}_-^{(i)}) \hat{\mathcal{E}}(\mathbf{r}_i) \quad (4)$$

where the system can be defined by the following quantities: $\omega_0 = 2\pi c/\lambda$ is the resonant frequency of the transition, $\hat{R}_3^{(i)}$ (with quantization axis along the z -direction) and $\hat{R}_\pm^{(i)}$ are quasi-spin operators for the i^{th} molecule in the sample, $\hat{a}_{\mathbf{k},\zeta}^\dagger$ and $\hat{a}_{\mathbf{k},\zeta}$ are the annihilation and creation operators for the wavevector \mathbf{k} , the index ζ denotes the polarization state, $\omega_k = kc$ are different mode frequencies, $\mathbf{d}^{(i)}$ is the dipole transition element for the i^{th} molecule, and $\hat{\mathcal{E}}(\mathbf{r}_i)$ is the quantized transverse electric field operator at the position of the i^{th} molecule [Benedict et al., 1996]. As first noted by Dicke [1954], superradiance is independent of the type of matter-radiation coupling. The interaction operator can either increase or decrease the spin quantum number of the system by one, which is equivalent to exciting a single molecule or inducing emission of a photon, respectively. Applying the Heisenberg equation results in [Gross and Haroche, 1982]

$$\frac{\partial \hat{\mathbb{N}}}{\partial \tau} = \frac{i}{\hbar} (\hat{P}_0^+ \hat{E}_0^+ - \hat{P}_0^- \hat{E}_0^-) \quad (5)$$

$$\frac{\partial \hat{P}_0^+}{\partial \tau} = \frac{2id^2}{\hbar} \hat{E}_0^- \hat{\mathbb{N}} \quad (6)$$

$$\frac{\partial \hat{E}_0^+}{\partial z} = \frac{i\omega}{2\epsilon_0 c} \hat{P}_0^-, \quad (7)$$

where the population inversion density of the medium is twice $\hat{\mathbb{N}}$. The operators \hat{P}_0^+ and \hat{E}_0^+ denote the envelope for the polarization and electric fields, associated with the general vectors (in the retarded frame, $\tau = t - z/c$)

$$\hat{\mathbf{P}}^\pm(z, \tau) = \hat{P}_0^\pm(z, \tau) e^{\pm i\omega\tau} \hat{\epsilon}_m \quad (8)$$

$$\hat{\mathbf{E}}^\pm(z, \tau) = \hat{E}_0^\pm(z, \tau) e^{\mp i\omega\tau} \hat{\epsilon}_m \quad (9)$$

with $\hat{\epsilon}_m$ representing the unit vector oriented with the molecular dipole moment. The radiation field here is assumed to propagate along the z -axis. A phenomenological addition of terms in the dynamic evolution equations for this system yield

$$\frac{\partial \hat{\mathbb{N}}}{\partial \tau} = \frac{i}{\hbar} (\hat{P}_0^+ \hat{E}_0^+ - \hat{P}_0^- \hat{E}_0^-) - \frac{\hat{\mathbb{N}}}{T_1} \quad (10)$$

$$\frac{\partial \hat{P}_0^+}{\partial \tau} = \frac{2id^2}{\hbar} \hat{E}_0^- \hat{\mathbb{N}} - \frac{\hat{P}_0^+}{T_2} \quad (11)$$

$$\frac{\partial \hat{E}_0^+}{\partial z} = \frac{i\omega}{2\epsilon_0 c} \hat{P}_0^- - \frac{\hat{E}_0^+}{L_{diff}} \quad (12)$$

with timescales of T_1 and T_2 accounting for population decay and dephasing, respectively, and L_{diff} as the characteristic diffraction length. Defining a cylindrical sample of radius w and length L as the large superradiant sample examined satisfying $L \gg w \gg \lambda$ (i.e. pencil-shaped), the superradiance time is derived to be

$$T_R = \tau_{sp} \frac{8\pi}{3\lambda^2 n L}, \quad (13)$$

in contrast with $T_R = \tau_{sp}/N$ for small samples ($V \lesssim \lambda^3$). In either case, the superradiance time decreases as the number of molecules cooperatively radiating increase in the sample. The condition

$$\frac{N}{Lw^2} < \frac{1}{\alpha a_0^2 \lambda} \sim \frac{1}{a_0^3}, \quad (14)$$

where α is the fine structure constant and a_0 the Bohr radius, ensures adequate spacing between neighbouring molecules by constraining the density of the medium. If this condition was not met, the analysis would have to be modified to account for short-range effects (e.g. dipole-dipole interactions) and wave function overlap. Another constraint imposed by the physical nature of superradiance is that $T_R > \lambda/c$ to ensure superradiance is not shorter than the optical period itself, otherwise this would prevent proximate molecules from developing coherence [Gross and Haroche, 1982]. Our analysis readily satisfies these conditions as it focuses on radio pulses emerging from low density environments with durations several orders of magnitude greater than $\nu^{-1} = \lambda/c$ (e.g. millisecond bursts for $\lambda \sim 18$ cm).

It is important to clarify that superradiance is distinct from amplified spontaneous emission (ASE): the process of a photon inducing de-excitation of inverted molecules via stimulated emission in a successive fashion to enhance power output more strongly than N independently radiating molecules. Superradiance differs fundamentally since it begins with an ensemble of fully excited molecules with permutation symmetry and aligned dipoles that must be treated as a correlated system. Both effects are collective and highly directional, but ASE exhibits no time delays in emissions, and the peak intensity no longer scales with N^2 [Bonifacio and Lugiato, 1975, Malcuit et al., 1987]. Superradiance is the transient limit in which the polarization envelope and inversion density change rapidly on the time scale of incoherent decay processes [Feld and Letokhov, 1980]:

$$\frac{\partial \hat{N}}{\partial t} \gg \frac{\hat{N}}{T_1} \quad (15)$$

$$\frac{\partial \hat{P}_0^+}{\partial \tau} \gg \frac{\hat{P}_0^+}{T_2}. \quad (16)$$

On the contrary, in the stimulated emission regime the polarization envelope and inversion density change slowly relative to incoherent decay rates. Although depending on dephasing phenomena in the environment which weaken correlations (e.g. electron exchange), these are competing effects [Maki et al., 1989].

After being theorized by Dicke, experimental confirmation of superradiance in optically pumped hydrogen fluoride gas was first published in 1973 [Skribanowitz et al.], with numerous subsequent laboratory observations in both gases and solids [Vrehen et al., 1977, 1979, Gounand et al., 1979, Raimond et al., 1982, Kaluzny et al., 1983, Florian et al., 1984, Andrianov et al., 1986, Eremenko et al., 1990, Zinoviev et al., 1991]. Recently, superradiance has been confirmed by Rajabi and Houde [2016b, 2017] in environments such as molecular clouds and circumstellar envelopes of evolved stars. The 21-cm line, a magnetic dipole transition, was analyzed considering circular polarization [Rajabi and Houde, 2016a] while other electric dipole lines (e.g. OH 1612 MHz) were investigated using a linear polarization state. These transitions were studied in regions presenting the conditions necessary for superradiance: a sufficiently dense sample of molecules, an inverted population, velocity coherence, and dephasing effects with time-scales longer than T_R . By identifying astrophysical sources exhibiting superradiance, this research corroborated the actuality of large-scale coherence in quantum systems naturally present throughout the universe. Based on data available, we believe extending this analysis of superradiance, although in different conditions, is applicable to describing the mechanism innate to cosmic fast radio bursts (FRB).

FRBs have been described as the most important enigma currently in astronomy with proposed origins ranging from neutron star collisions to primordial black holes to extraterrestrial communication. The Lorimer Burst was a 5-millisecond radio burst measured in 2001 and regarded as the first recorded observation of FRBs [Lorimer et al., 2007]. There have been 21 distinct FRBs detected as of today yet the mechanism(s) behind their origins remain unknown. Although seemingly rare and only relatively recently discovered, findings imply an FRB is detectable on Earth once every 10 seconds, which suggests FRBs are not emerging from cataclysmic events but instead are arising from conditions that should be prevalent throughout the universe as they are also assumed to be extragalactic [Champion et al., 2016, Lyutikov et al., 2016]. And although no two FRBs are identical, they share a few remarkable similarities. The large luminosities yet small durations of FRBs imply candidate sources are both compact and rely on an energetic process, possibly linked to coherent radio waves [Thornton et al., 2013, Luan and Goldreich, 2014]. FRBs are thought to be broadband signals with a wave frequency on the order of GHz and pulse durations on the order of milliseconds as shown in Figure 2. Their high dispersion measure, $DM = \int_0^L n_e dz$, where n_e is the electron density along the path travelled by the photon to an observer, also indicates an integrated electron column density on the order of 10^4 pc cm^{-3} ($\sim 10^{26} \text{ m}^{-2}$) [Hilmarsson, 2015]. To observe such large DM indicates these signals must be extragalactic. Rotation measures (RM) for FRBs, which are based on the detected polarization angle at different observing frequencies, also enable estimates of net magnetic fields permeating the intergalactic medium [Ravi et al., 2016].

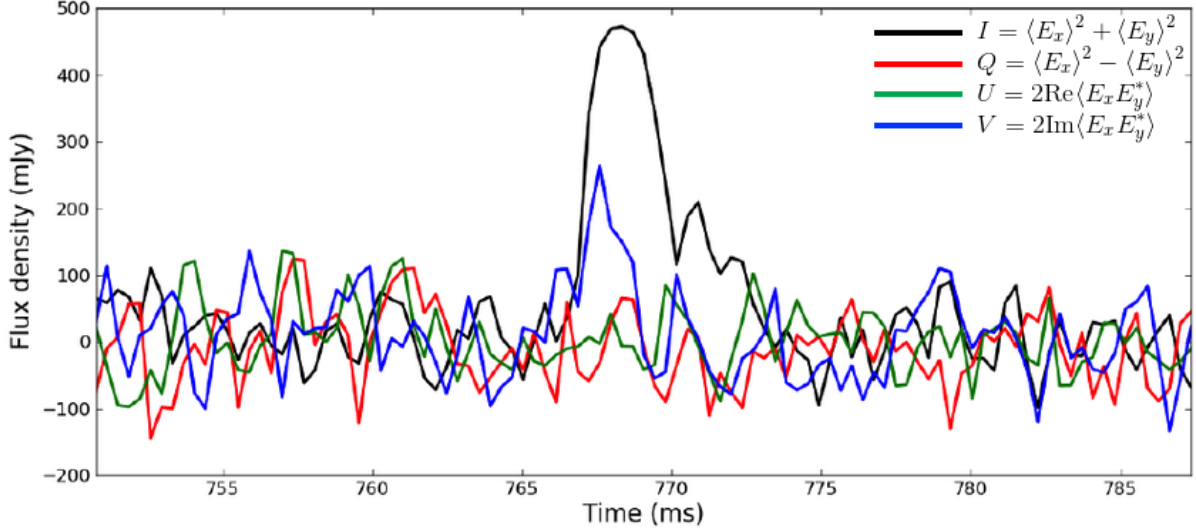


Figure 2. Smoothed data of FRB 140514¹ with corresponding Stokes parameters displaying strong pulses with ringing features. Copyright © 2017 [Petroff et al., 2015].

One peculiarity in observations appears to be repeatability: at least for some class of FRBs, it is expected that the environment permits repetition of the event. This is indicated by observations of the single known repeating signal, FRB 121102, which has been observed on 17 separate occasions alone [Scholz et al., 2016]. Consistency in dispersive indices reveal a single source is likely responsible for the events as well. Thus repetitiveness is a property of this specific FRB, therefore excluding violent events (e.g. blackhole merger) as its progenitor. Also, no periodic structure has been identified in any FRB to date [Spitler et al., 2016]. Another anomaly is that some FRBs even display a double-pulsed profile which is not well understood and not widely observed, although it is speculated these multiple-component bursts may simply be unresolved in some other FRBs due to intrachannel smearing and scattering [Champion et al., 2016]. Furthermore, intrinsic polarization has also been observed in some FRBs with Ravi et al. [2016] reporting a linear polarization of 80% for FRB 150807. In certain previous observations, lack

¹FRB naming system is “YYMMDD” (e.g. a detection on 30 August 2010 is designated as FRB 100830).

of polarization detection may have resulted from Faraday rotation when the signals propagated through strong magnetic fields or sufficiently dense mediums [Petroff et al., 2015]. Coupled with the above properties, the exceptionally bright fluxes (up to $\sim 10^2$ Jy) when observed from sources suspected to be billions of parsecs away constrain possible mechanisms, but we believe coherent radiation arising from superradiance adequately satisfies the above description. The following analysis of superradiance investigates the parameters outlined above (e.g. signal frequency, pulse durations) to hopefully enlighten research on these perplexing bursts.

Solving the system of coupled partial differential equations (PDE) given by (10)–(12) governing the time and spatial evolution of \hat{N} , \hat{P}_0^+ , and \hat{E}_0^+ require the implementation of a suitable numerical technique. One finite difference approach to numerically integrate these equations is the method of lines which discretizes all but a single independent variable; this procedure converts a PDE into a system of ordinary differential equations (ODE), upon which applicable solvers are tested. In particular, an adaptive step using the Cash-Karp method which computes fourth- and fifth-order accurate solutions and compares their differences to adjust the step size (based on an initially specified tolerance) is a potential integration routine examined. Backward differentiation formula (BDF), a class of implicit numerical schemes, are also reviewed due to the possibly stiff nature of the output—that is the field and molecular observables may display oscillations corresponding to widely varying spatial lengths and timescales (the adaptive step becomes increasingly small in these regions) [Gear, 1971]. Thus convergence tests with differing techniques are sought when testing code. Variant and unconventional approaches to the method of lines are also considered (e.g. advancing \hat{E}_0^+ in z), and all of this must be completed using an appropriate platform.

Python is an interpreted, dynamically-typed, open-source programming language with efficient

array manipulation and data modelling packages. For these reasons, Python is the primary programming language employed for this numerical study. Independently constructed codes and public libraries are investigated and their associated output can be compared to simulations from existing operational code only applicable to particular cases (e.g. sine-Gordon solution [Burnham and Chiao, 1969]) to assess the stability and accuracy properties of newly applied computational methods. Conducting these simulations extends the scope of superradiance analysis to study coherent radiation events emerging in quite variable conditions suspected for FRBs. Such work will provide insight into potential mechanisms for these flares.

Methodology

The methods applied for this project in modelling one-dimensional superradiance are predominantly computational in nature building upon theory that has been further developed since Dicke first proposed superradiance [Burnham and Chiao, 1969, Arecchi and Courtens, 1970, Feld and Letokhov, 1980, MacGillivray and Feld, 1981, Gross and Haroche, 1982, Benedict et al., 1996]. To numerically model the quantum mechanical evolution of the system, equations (10)–(12) must be replaced with semi-classical equations which substitute the slowly-varying quantum operators with the classical quantities $\mathcal{N}_{cl}(z, \tau)$, $\mathcal{P}_{cl}(z, \tau)$, and $\mathcal{E}_{cl}(z, \tau)$. Solving these equations for a particular set of random initial conditions corresponds to a single classical trajectory or realization; to find the expectation value, the weighted average of numerous classical trajectories is needed.

The Python script I independently created to model superradiance solves the corresponding semi-classical equations. To convert this set of PDEs to a system of ODEs and apply established numerical integration methods, a discretization scheme similar to the method of lines is

utilized where a Cartesian grid composed of the spatial coordinate, z , and temporal coordinate, τ , are divided evenly into an $A_z \times B_\tau$ mesh (A_z indicates the number of spatial divisions and B_τ the number of temporal divisions). With this grid, a 4th-order Runge-Kutta method was employed to solve the system of equations and the electric field was advanced in z while both the population inversion and polarization were advanced in τ at each grid point. In determining the dimensions of the simulated mesh, the axes ranged from $0 \leq z \leq L$ and $0 \leq \tau \leq \tau_{\max}$, implying that $\Delta z = L/A_z$ and $\Delta \tau = \tau_{\max}/B_\tau$. In this approach, the code marches forward along a particular grid line (i.e. $z_k = k\Delta z$) in τ and at each point \mathcal{E}_{cl} is computed at the next grid point in z , while \mathcal{N}_{cl} and \mathcal{P}_{cl} are computed at the next grid point in τ . This takes place until the code reaches the final grid point in τ at the particular z_k , and then shifts to the next line at z_{k+1} by taking one step of size Δz and starting at $\tau = 0$ again. The code then marches along the gridline to $\tau = \tau_{\max}$ again, and this process continues throughout the entire grid. This method is valid in our modelling of superradiance in astronomical settings because it assumes the backward propagating wave is negligible, which is the case in superradiant systems inverted by longitudinal pumping in a mirrorless environment [Haroche et al., 1977]. Also, variables were rescaled throughout the code to ensure 64-bit floats for each of the real and imaginary parts were sufficient to store computed values in memory. Initial and boundary conditions determine the evolution of the system, and the ones applied were:

$$\mathcal{N}_{cl}(0, \tau) = \frac{N}{2V} \cos(\theta_0) e^{-\tau/T} \quad (17)$$

$$\mathcal{N}_{cl}(z, 0) = \frac{N}{2V} \cos(\theta_0) \quad (18)$$

$$\mathcal{P}_{cl}^+(0, \tau) = \frac{Nd}{2V} \sin(\theta_0) e^{-\tau/T} \quad (19)$$

$$\mathcal{P}_{cl}^+(z, 0) = \frac{Nd}{2V} \sin(\theta_0) \quad (20)$$

$$\mathcal{E}_{cl}^+(0, \tau) = 0 \quad (21)$$

$$\mathcal{E}_{cl}^+(z, 0) = 0 \quad (22)$$

where $\bar{\theta}_0 = 2/\sqrt{N}$ is the mean initial tipping angle describing the inversion and initial polarization as per the Bloch vector. (Whether θ_0 equals $\bar{\theta}_0$ exactly or fluctuates around this mean value, the dynamics of the system are fairly similar and results in a macroscopic dipole as shown in Figure 3.) The electric field amplitude is zero initially and the small polarization is instead used to approximate quantum fluctuations in the semi-classical equations that will eventually initiate superradiant emission by creating a macroscopic dipole [Gross and Haroche, 1982]. Using the retarded time in this code is particularly insightful as it permits the initial conditions to be set based on the longitudinal pumping pulse that travels through the axis of the medium and can leave behind a homogeneous concentration of inverted molecules [Laptev et al., 1984]. For a superradiant sample of length L , the propagation time, $\tau_E = L/c$, necessary to establish coherence through the sample is not required to be shorter than T_1 or T_2 when operating in the regime of swept excitation. Although T_R must still be shorter than the dephasing and relaxation times, and this will affect the ringing observed as the superradiant envelope trails very closely behind the pumping pulse.

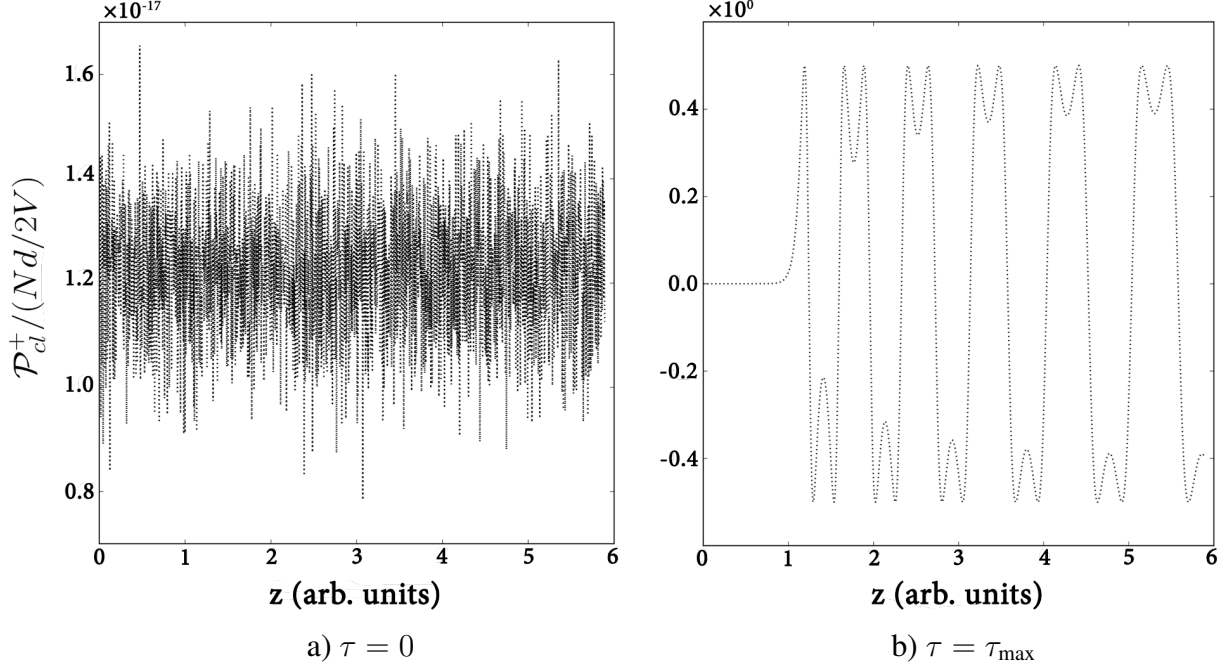


Figure 3. Initially uncorrelated molecular polarization which ultimately leads to a macroscopic dipole due to phase-locking between the spatially separated molecules and the radiation field.

In our code there is quite a bit of flexibility as one can arbitrarily vary parameters such as T_1 , T_2 , L_{diff} , and θ_0 at any point in z and τ . The numerical model accounts for a characteristic diffraction length of roughly $FL/0.35$ in this sample, where $F = \frac{A}{\lambda L}$ is the Fresnel number [Gross and Haroche, 1982]. Pumping reservoirs and loss terms can also be added to represent potential sources in the environment. Multiple realizations can be tested as well where input parameters such as T_R and n can vary (e.g. Gaussian distributed); the code runs each realization and combines the intensity of each one to find the final emitted pulse. For cases in this thesis considering multiple samples (i.e. Figures 8 and 9), the solutions were typically found to converge after one thousand realizations were simulated. When testing this code and comparing it to the particular cases where the sine-Gordon equation is valid [Rajabi and Houde, 2016a,

2016b], results were found to be in good agreement.

To compute power spectra, the FFT library from `SciPy` was imported. Visualization was possible through use of `matplotlib`, where particular slices can also be chosen to display the evolution of the operators at a particular τ or z . The package `tqdm` was also helpful in ascertaining the speed and progress of the code as it provides a completion bar which is extremely useful when running it on SHARCNET (i.e. remote clusters), increasing the number of realizations, and using finer meshes. For improved performance, an analogous code has been created in C++.

One approximation applied in the field equation is the slowly varying envelope approximation (SVEA), which assumes

$$\left| \nabla^2 \hat{E}_0^+ \right| \ll \left| k_0 \nabla \hat{E}_0^+ \right| \quad (23)$$

$$\left| \frac{\partial^2 \hat{E}_0^+}{\partial t^2} \right| \ll \left| \omega_0 \frac{\partial \hat{E}_0^+}{\partial t} \right| \quad (24)$$

and essentially neglects second-order derivatives in the field and molecular operators. To comment on alternative numerical approaches attempted and considered: initially a non-SVEA code employing the adaptive Cash-Karp method was being developed. Although it was found that the SVEA code is apt to simulate millisecond pulses from radio waves in the GHz frequency range since the SVEA approximation breaks down only when T_R is smaller than $\lambda/c \sim 10^{-11}$ s. Even with persistent ringing and multiple realizations, it is unlikely that the observed pulse is 10^8 times longer than T_R . Furthermore, Gross and Haroche [1982] note that such a duration for T_R is not physical as it would indicate inversion in the medium being realized in a time shorter than the optical period of the electromagnetic wave itself. For the SVEA case, an adaptive mesh using the Cash-Karp method was also tested instead of using a constant interval spacing,

although this was ultimately removed as it was largely unnecessary in this problem because the initial/boundary conditions applied led to non-stiff behaviour in the solutions. Using pre-determined constant mesh sizes allowed for consistency when testing the code while varying parameters (i.e. less changing variables when testing the code). And using the explicit 4th-order Runge-Kutta method (as opposed to implicit methods, e.g. BDF) was perfectly adequate for this problem as long as the variables were properly scaled as to avoid any stability issues when taking time- and spatial-steps.

Discussion

In uniform or transverse pumping—where an entire system is inverted simultaneously—the Arecchi-Courtens condition requires $L/c < T_R$ in order for coherence to develop throughout the superradiant sample. Violating this condition can result in separate parts of the medium emitting photons before interacting with each other, altering the emitted burst’s temporal width [Arecchi and Courtens, 1970, Gross and Haroche, 1982]. Although when considering large samples on the order of milliparsecs in length, the Arecchi-Courtens condition is not necessary in systems prepared by swept excitation because molecules are only inverted when the pumping pulse propagating through the medium arrives at its position. Therefore, depending on the characteristics of the longitudinal pumping source, the cooperation length can theoretically be infinite [Bonifacio et al., 1975, Haroche et al., 1977]. In astronomical environments, the conditions necessary for superradiance share similarities with masers that are naturally occurring throughout the universe, and superradiance has been observed in known masing regions [Rajabi and Houde, 2016a, 2016b, 2017]. Pumping processes responsible for the enhanced emission in masing regions on the timescale of days to months are primarily due to radiative and collisional pumping [Goldreich and Kwan, 1974]. An OH maser stimulated by a neighbouring pulsar with

emission time on the order of milliseconds has been observed as well [Weisberg et al., 2005]. This can similarly occur in superradiance whereby a system of inverted molecules can be triggered by a small external pulse; this can be viewed as the nonlinear coherent amplification of the triggering photons and has been observed experimentally. Semi-classical theory models this process well because the burst emission is initiated by a classical external field instead of quantum fluctuations [Benedict et al., 1996]. In any case, a sufficiently strong (perhaps repeating) swept excitation from an external radiative pump can interact with the molecules such that the system bursts cooperatively to produce exceptional intensities [Rajabi and Houde, 2017].

Although exact environments for FRBs are not yet well-determined, conditions near active galactic nuclei (AGN) of luminous infrared galaxies where beamed emission from megamasers and gigamasers have been observed are one possibility [Booth and Aalto, 1998, Lockett and Elitzur, 2008] as a persistent radio source believed to be an AGN has been co-localized to FRB 121102 [Chatterjee et al., 2017]. In past surveys of roughly 200 hours of telescope time at the Arecibo Observatory, about 300 (extragalactic) OH megamasers were observed associated to AGN, suggesting velocity coherence in large radiating gas clusters is ubiquitous near the centres of galaxies [Darling and Giovanelli, 2002]. These OH megamasers have compact regions that can be radiatively pumped where $L \sim 1$ pc and $n \sim 10^{-1} \text{ cm}^{-3}$ [Kylafis and Pavlakis, 1998]. And because of the limit on angular size, no radio sources besides pulsars and certain masers are known to exhibit both diffractive and refractive scintillation [Narayan, 1992]. In this domain of strong scattering, multi-path propagation can arise as seen in some FRBs [Masui et al., 2015, Ravi et al., 2016].

Masers operate in the steady-state regime where the intensity is proportional to the inversion rate. An important consideration by Elitzur [1992] is that coherence cannot generally be es-

tablished in inverted mediums through stimulated emission alone: if a photon is emitted at an angle, β , to the z -axis, then over a sample's length the phase difference accumulated will be given approximately by $\frac{L}{\lambda}\pi\beta^2$. To ensure only a small phase difference accrues for radiation wavelengths $\lambda \sim 18$ cm across a distance of $L \sim 10^{18}$ cm (arbitrary upper limit), β should be smaller than 10^{-8} rad. Therefore masers arising from stimulated emission are unlikely to produce the narrow beaming angles necessary to preserve phase coherence. Superradiant evolution on the other hand naturally develops strong angular correlations because of the electric dipole interactions between molecules. The probability of a photon being emitted with the same mode as incoming photons is magnified when considering the interaction of all the superradiant photons emitted from previous molecules versus just two photons in ordinary stimulated emission [Rajabi and Houde, 2016a]. Cooperative emission thus tends to proceed along narrow geometries and triggers phase-matching of radiation from different molecules. With such angular correlations, for a pencil-shaped superradiant sample with Fresnel number near unity, it is possible for molecules to develop coherence with a swept pumping source as photons are emitted in a solid angle of approximately λ^2/A [Gross and Haroche, 1982]. It is worth noting that swept excitation eases the length requirement of $L < c\Delta t \sim 10^8$ cm [Lyutikov et al., 2016, Ravi et al., 2016] stated for FRBs with millisecond durations since T_R scales proportionally to $1/nL$ if $F \sim 1$, which is assumed below. (If $F \leq 0.1$, then T_R is proportional to $1/nA$ [MacGillivray and Feld, 1981].) And if longitudinally excited by sources such as shock fronts which are naturally sheet-like [Elitzur, 1992], numerous superradiant filaments will likely arise as displayed in Figure 4.

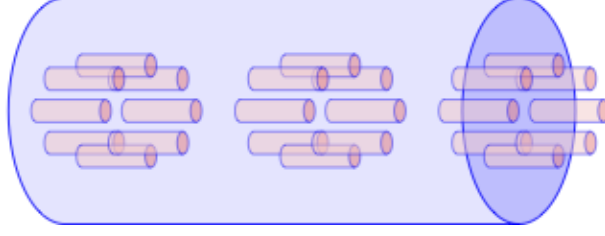


Figure 4. Visualization of multiple superradiant samples (of varying dimensions) that can be realized through inversion by just a single swept pumping source (courtesy of F. Rajabi).

Since the propagation time to an observer on Earth is constant for all samples inverted by a single source, only the delay time, $\tau_D \simeq \frac{T_R}{4} |\ln(\frac{\theta_0}{2\pi})|^2$, necessary for superradiance to emerge will differ among various realizations. Intensity fluctuations (or ringing effects) are visualized in Figure 5 representing the reabsorption and re-emission of photons throughout the sample for just one realization. The final weaker bursts come from a lower number of cooperating molecules as the population inversion is depleting. Although ringing will be suppressed if T_1 is short enough.

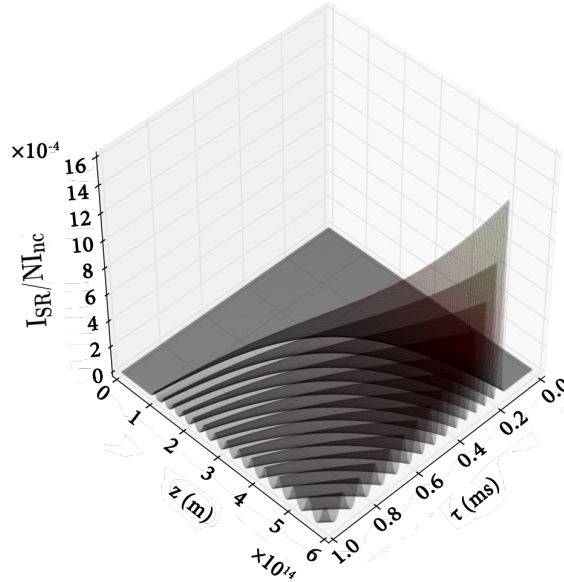


Figure 5. Superradiance intensity scaled to ideal sample emission, NI_{nc} , where $I_{nc} = \frac{2}{3} \hbar \omega / AT_R$, $\langle nL \rangle \sim 2 \times 10^{-3} \text{ cm}^{-3} \text{ pc}$ and $T_1, T_2 \gg T_R$ using 1720 MHz OH transition.

Focusing now on FRB 150807, which was detected using the 64-m Parkes radio telescope, it has a bandwidth-averaged peak flux density of 120 Jy with a spectrum that is strongly enhanced between the observing frequencies of 1250–1300 MHz. The closest counterpart found to FRB 150807 was the bright galaxy VHS7 which has an estimated redshift of $z = 0.32$ and inferred luminosity distance of 1.7 Gpc [Ravi et al., 2016] implying a peak frequency near 1720 MHz local to the source of the burst itself. This frequency corresponds to the OH satellite transition ($^2\Pi_{3/2}, J = 3/2, F = 2 \rightarrow 1$) in the molecule’s ground rotational state, which can be readily inverted by far-infrared radiation [van Langevelde et al., 1995]. Since FRB 150807 is relatively well-constrained in distance because of its high observed brightness and real time detection, we adopt the 1720 MHz OH line in our analysis of FRBs. Although parameters in our model of superradiance must be slightly adjusted for different molecular lines, the dynamics of radio transitions will be similar (assuming similar environments and pumping effects).

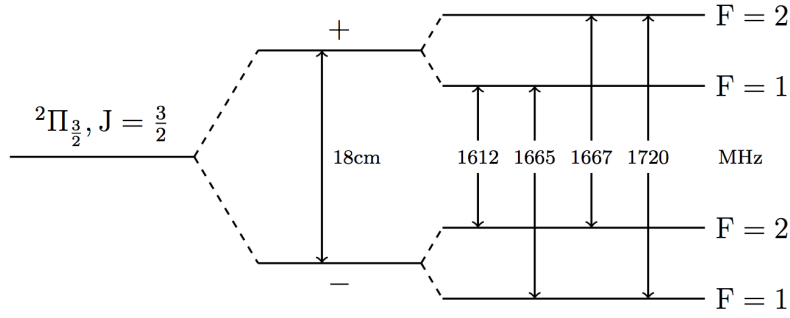


Figure 6. Orbital splitting arising from interaction of rotational and electronic angular momenta of an OH molecule creates \pm states. Additional splitting from electron and nuclear spin interactions in the hydrogen atom results in hyperfine levels in the 18-cm line. Figure taken from [Rajabi and Houde, 2016b].

Before proceeding it is important to review a few broadening mechanisms since a constraint on superradiance is that dephasing and relaxation times should be longer than T_R . This is

readily satisfied for collisional broadening when noticing T_R is significantly smaller than the dominating OH–H₂ collision times near AGN given by $T_C = 1/n_{\text{H}_2}\sigma_g\bar{v}$, where the geometrical cross-sectional area of a hydrogen molecule, σ_g , is approximately $4 \times 10^{-16} \text{ cm}^2$. At $T \sim 100 \text{ K}$ and $n_{\text{H}_2} = 10^4 \text{ cm}^{-3}$, T_C is calculated to be nearly 10^6 s [Alatalo et al., 2011, Rajabi and Houde, 2016b]. Doppler broadening resulting from motions of molecules in thermal equilibrium cause variations in the absorbing frequency given by $\Delta\nu_D = \frac{\nu_0}{c} \sqrt{\frac{2kT}{m}}$. Although these regions near AGN are out of equilibrium, a thermally relaxed gas of OH provides a rough estimate for maximum dephasing of $T_2 = 1/\Delta\nu_D = 500 \mu\text{s}$ at 100 K. Since $T_2 \propto T^{-1/2}$, superradiance can sustain environments in even higher temperatures as long as $T_2 > T_R$. Dipole-dipole interactions do not disrupt coherence if the molecular density is low enough (e.g. $n \sim 10^{-1} \text{ cm}^{-3}$) in these environments. Kylafis and Pavlakis [1998] also find that megamaser gas clusters of 1 pc are observed to have velocities ranging from a few hundred to thousands of km/s leading to frequency widths of approximately $10^5 - 10^6 \text{ Hz}$ at least for megamasers [Baan and Klockner, 2001, Lo, 2005]. The line profiles of these OH megamasers display a variety of shapes that are often quite complex, too [Lonsdale, 2002]. Along with thermal effects, natural broadening can lead to structure on the order of 10–100 kHz as the inner ringing components of superradiant bursts can have widths ranging from 10–100 μs . Such small-scale structures in spectra have been observed in FRB 150807, although further evidence is needed before claiming whether these bandwidths are related to scattering events or intrinsic to the FRB mechanism itself.

It is also known that splitting of energy levels in an ensemble of molecules due to a uniform external electric field of amplitude E_0 produces a line width of dE_0/\hbar due to the Stark effect. FRBs are broadband and we believe such spectra can be derived when considering Rabi oscillations in a system of N coherently radiating molecules with an oscillating electric field. This could yield sufficient broadening in the presence of strong electric fields, but can lead to the

suppression of collective resonance as well [Slysh, 1973, Svidzinsky et al., 2013]. Nevertheless, the influence of Rabi oscillations on a superradiant system is still being investigated. This is an aspect of the model that will be delved into in future work.

An exponential tail has been observed in certain FRBs which has been proposed to arise largely from scattering from both the host galaxy and intergalactic medium to varying degrees [Thornton et al., 2013, Ravi et al., 2015, Masui et al., 2016]. Superradiance does not exclude this possibility, but depending on dephasing and relaxation phenomena, the observed tails can arise naturally in superradiant bursts. As displayed in Figure 7, the envelope of the ringing for a single realization follows an exponential curve with spectral features on the order of 50 kHz. The rapidly varying ringing components found in superradiance can be even shorter in time at larger column densities and ringing may be responsible for the peculiar small scale structures observed in certain FRBs [Ravi et al., 2016].

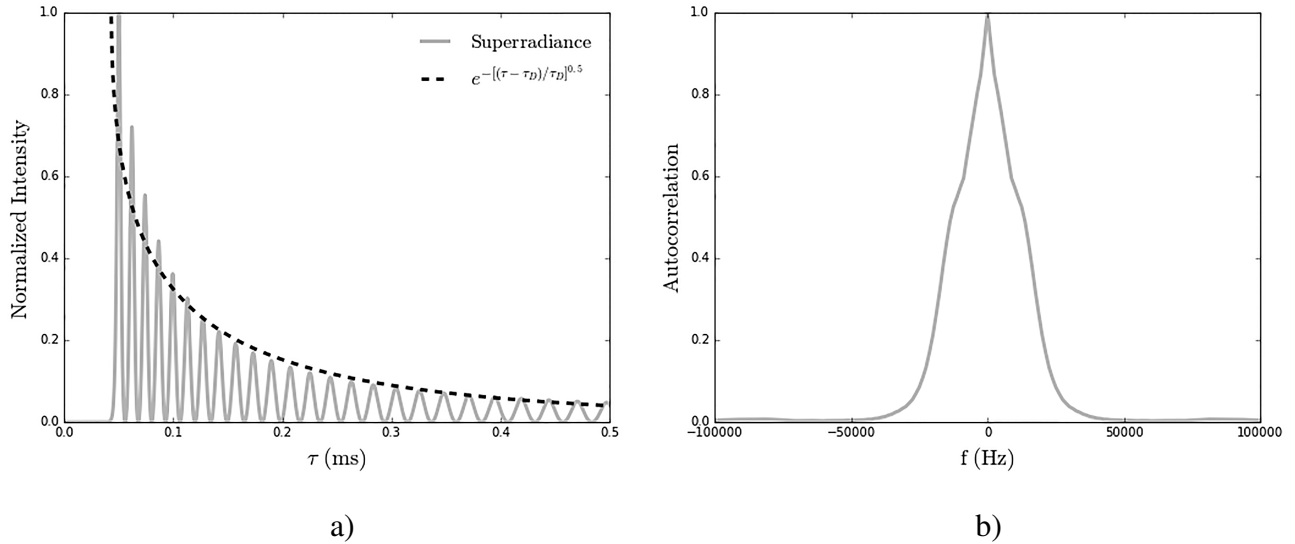


Figure 7. A single realization indicating small scale structure can be present when $T_R = 0.1 \mu\text{s}$ and $T_1, T_2 \gg T_R$, where (a) displays the single emitted signal in time with an exponential tail and (b) the frequency-autocorrelation of the power spectrum.

When multiple realizations spring up as expected, the observed signal is broadened and can closely match features observed in these extragalactic bursts. For example, the pulse widths and intensities themselves correspond similarly to that observed for FRB 110220 when simulating multiple realizations as demonstrated in Figure 8, which superposes our simulations to the observed total flux density which has a signal-to-noise ratio (SNR) of 49 and time resolution of 0.8 ms. This burst exhibits two maxima along with a tail that steadily decreases with ringing from the numerous composite realizations smeared out with mean inverted column density $\langle nL \rangle \sim 6 \times 10^{-5} \text{ pc cm}^{-3}$.

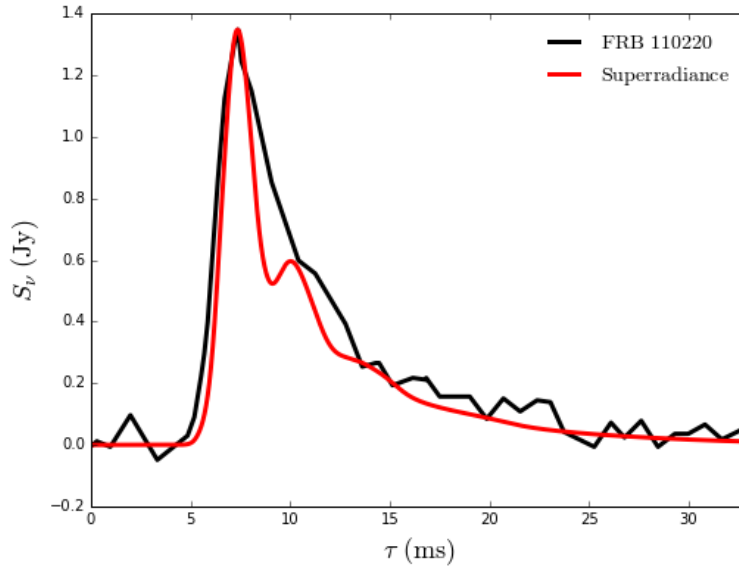


Figure 8. Superradiance with similar ringing features to the total intensity of FRB 110220.

For the simulations $\langle T_R \rangle = 15 \mu\text{s}$, $\langle n \rangle = 10^{-1} \text{ cm}^{-3}$, and $T_1 = T_2 = 1000\langle T_R \rangle$, where

$$\sigma_{T_R} = 0.07\langle T_R \rangle \text{ and } \sigma_n = 0.07\langle n \rangle. \text{ Data taken from Thornton et al. [2013].}$$

It is also possible for the emitted pulse to be more symmetric if T_1 and T_2 are shorter. FRB 150418 has a pulse width of $0.8 \pm 0.3 \text{ ms}$ but the intrinsic width is likely unresolved due to dispersion smearing from the finite frequency resolution of the spectrometer [Keane et al., 2016].

Our superradiance framework can reproduce the observed pulses if $\langle nL \rangle \sim 0.1 \text{ pc cm}^{-3}$ as displayed in Figure 9, and shorter burst widths are possible at larger column densities. Although the energy stored in the superradiant system is not starkly different from a similarly inverted sample (i.e. same dimensions and molecular density), the high intensities simply correspond to the system releasing its energy in short durations and a small beaming angle characteristic of superradiant emission. No significant linear or circular polarization was observed in FRB 150418, and it is possible an absence of net polarization is caused by factors such as: multiple transitions/realizations arising, background radio emission, and scattering effects from intergalactic propagation.

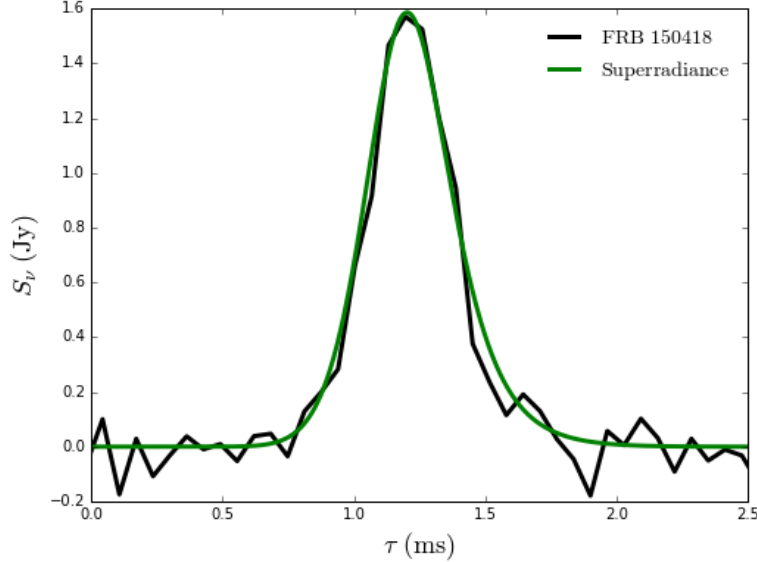


Figure 9. Total flux density observed for FRB 150418 compared to superradiance model using

$$\langle T_R \rangle = 1.4 \mu\text{s}, \langle n \rangle = 10^{-1} \text{ cm}^{-3}, \sigma_{T_R} = 0.01 \langle T_R \rangle, \sigma_n = 0.01 \langle n \rangle, \text{ and } T_1 = T_2 = 500 \langle T_R \rangle.$$

FRB 150418 data courtesy of Keane et al. [2016].

FRB 121102 has also been observed to repeat from a suspected single region in the sky [Spitler et al., 2016]. This implies that for at least one class of FRBs, the mechanism cannot be cataclysmic. This follows naturally with the above superradiance framework which can permit

both single and repeating bursts if another swept pumping pulse inverts the sample once again. Such conditions and pumping could be realized near a potential AGN which is projected to be separated by less than 40 pc from FRB 121102 [Marcote et al., 2017]. For the distinct bursts detected from this source, the observed signals' peak frequencies are not constant, indicating the possibility that different molecular/atomic species are involved. In the past both methanol and water lines were detected from a single astronomical superradiant region and thus the interplay of multiple transitions is not precluded [Rajabi and Houde, 2017]. It is also possible these frequency differences appear due to relative velocities of the radiating regions themselves. Extragalactic OH emissions have been observed to have velocity widths of 2.2×10^3 km/s alone [Baan and Klöckner, 2001], and regions receding or approaching Earth at potentially higher velocities could produce large Doppler shifts. Velocity widths from different superradiant realizations moving at relativistic speeds are not ruled out.

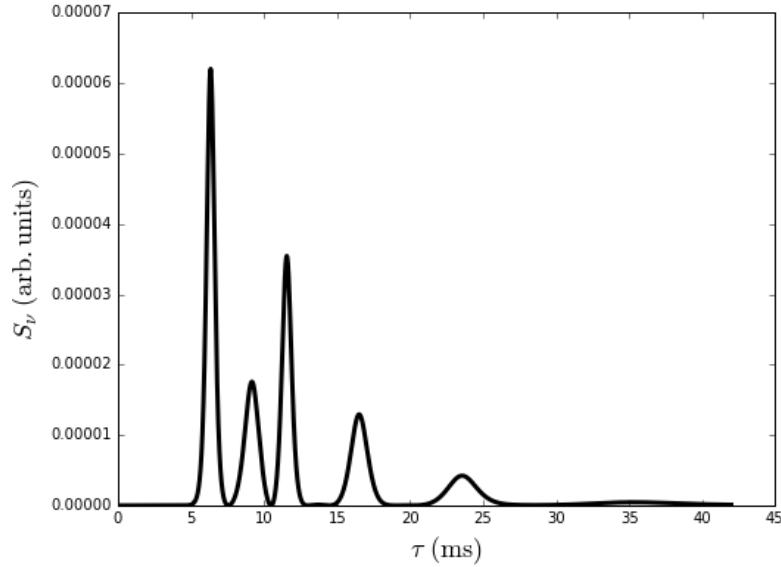


Figure 10. Multiple-peaked superradiance with bursts separated in time arising from a single realization using $T_R = 14 \mu\text{s}$, $n = 10^{-1} \text{ cm}^{-3}$, $T_1 = 40 \text{ ms}$, and $T_2 = 4 \text{ ms}$.

The double peaked nature of certain FRBs can also be explained in our model. This arises naturally if two separate pumping pulses trailing behind one another can prepare the system to burst again (i.e. rapid repetition in superradiance). Another possibility is that proximal superradiant systems could longitudinally pump the regions ahead of them, leading to slightly different τ_D accumulating for different trajectories which would then emit pulses which are slightly offset in time. Perhaps the simplest explanation arises from a single superradiant system—where T_1 is quite longer than T_2 —retaining inversion even after the first pulse, and emitting a second pulse shortly afterwards as demonstrated in Figure 10. The behaviour could be further modified if n , T_1 , T_2 , and/or L_{diff} themselves vary throughout the sample’s length as well, and if quantities in different realizations (e.g. molecular density) are not necessarily varying based on a Gaussian distribution. Non-uniform boundary/initial conditions with regards to the polarization and population inversion density could be applied for the numerous realizations possible, which could lead to altered pulse shapes, too.

It is worth noting that the double-peaked pulses appear to blend together into a single peak for FRBs observed at lower frequencies. Also, the intrinsic widths of FRBs appear to differ depending on the observing telescope used. For example, FRB 121102 is the only repeating FRB observed out of the 21 distinct ones [Petroff et al., 2016], and followup studies at the Arecibo telescope found longer intrinsic temporal widths ranging from 3–9 ms for FRB 121102 compared to observations at the Parkes telescope which found a lower limit on the range of observed burst widths to be 0.6 ms [Scholz et al., 2016]. The possibility of more than one type of FRB source being present in this region cannot be excluded. These findings suggest that the local environment, propagation, and detector effects all influence our understanding of the emitted pulse to different extents and require further investigation to determine which observed properties are extrinsic to the burst mechanism. As new information is arriving to help elucidate

the above findings, this will improve parameters and initial/boundary conditions applied in our simulations.

Conclusion

Through analysis of expected naturally occurring large-scale quantum entangled regions of molecules with novel simulations, this work finds that superradiance in astronomical environments permits the emergence of transient radio signals. Large cylindrical samples with aligned dipoles pumped through swept excitation can radiate cooperatively and produce the observed and expected characteristics of FRBs: exponential tail behaviour, small scale structure, repeatability, multiple peaks, exceptional intensities, millisecond widths, and ubiquity. All that is needed for these molecules to radiate coherently as a single quantum system are velocity coherence, sufficient density, and population inversion.

Other candidate transitions for superradiance to yield FRBs still remain to be investigated such as the 21 cm line. Future work also needs to be carried out on deriving spectra corresponding to superradiant systems in the presence of external electromagnetic fields that can broaden observed frequencies. Upcoming endeavours such as the Canadian Hydrogen Intensity Mapping Experiment (CHIME) and Deep Synoptic Array prototype are expected to further enlighten research on FRBs to help determine whether superradiant regions are responsible for these transient radio signals.

Acknowledgments

I am grateful for Fereshteh Rajabi's and Martin Houde's immense support throughout this project as this work would not have been possible without their efforts. I also thank Evan Keane for providing his data on FRB 150418 for the analysis.

References

- K. Alatalo et al. Discovery of an AGN-driven molecular outflow in the local early-type galaxy NGC 1266. *The Astrophysical Journal*, 735(2):88, April 2011.
- S. Andrianov et al. Optical superradiance in a diphenyl crystal with pyrene. *Soviet Physics Uspekhi*, 29(11): 1060, 1986.
- F. T. Arecchi and E. Courtens. Cooperative Phenomena in Resonant Electromagnetic Propagation. *Physical Review A*, 2(5):1730, November 1970.
- F. T. Arecchi et al. Atomic coherent states in quantum optics. *Physical Review A*, 6(6):2211, December 1972.
- W. A. Baan and H. R. Klöckner. Properties of OH megamasers and ultra-luminous infrared galaxies. In *ASP Conference Series, Astronomical Society of the Pacific, Volume 249. 2001, San Francisco, California, U.S.A., page 639, 2001.*
- M. G. Benedict et al. Microwave emission from a crystal of molecular magnets: The role of a resonant cavity. *Physical Review B*, 72:214430, December 2005.
- M. G. Benedict et al. Super-radiance Multiatomic Coherent Emission. Bristol: IOP Publishing Ltd, 1996.
- R. Bonifacio and L. A. Lugiato. Cooperative radiation processes in two-level systems: Superfluorescence. *Physical Review A*, 11(5):1507, 1975.

- R. Bonifacio and G. Preparata. Coherent spontaneous emission. *Physical Review A*, 2(2):336, 1970.
- R. Bonifacio et al. Steady-state pulses and superradiance in short-wavelength, swept-gain amplifiers. *Physical Review A*, 12:2568, December 1975.
- R. S. Booth and S. Aalto. Molecular gas, starbursts and active galactic nuclei, T.W. Hartquist and D. A. Williams, eds. *The Molecular Astrophysics of Stars and Galaxies*, p.437, Oxford: Clarendon Press, 1998.
- D. C. Burnham and R. Y. Chiao. Coherent resonance fluorescence excited by short light pulses. *Physical Review*, 188(2):667, December 1969.
- D. J. Champion et al. Five new fast radio bursts from the HTRU high-latitude survey at Parkes: first evidence for two-component bursts. *Royal Astronomical Society*, 460(1):L30–L34, April 2016.
- S. Chatterjee et al. A direct localization of a fast radio burst and its host. *Nature*, 541:58–61, January 2017.
- J. Darling and R. Giovanelli. A Search for OH Megamasers at $z > 0.1$. III. The Complete Survey. *The Astronomical Journal*, 124(1):100–126, July 2002.
- R. H. Dicke. Coherence in spontaneous radiation processes. *Physical Review*, 93(1):99, 1954.
- M. Elitzur. *Astronomical masers*, volume 170 of *Astrophysics and Space Science Library*. Dordrecht: Kluwer, 1992.
- D. Engels, and F. Brunzel. A database of circumstellar OH masers. *Astronomy & Astrophysics*, 582:A68, October 2015.
- V. Eremenko et al. Optical superradiance in crystals—method of relaxation process studies. *Journal of Molecular Structure*, 219:189–197, 1990.
- M. S. Feld and V. S. Letokhov. Coherent nonlinear optics. *Topics in Current Physics*, Springer-Verlag Berlin Heidelberg New York, 1980.

- R. Florian, L. Schwan, and D. Schmid. Two-color superfluorescence of O_2^- centers in KCl. *Journal of Luminescence*, 31:169–171, 1984.
- C. W. Gear. Simultaneous numerical solution of differential-algebraic equations. *IEEE transactions on circuit theory*, 18(1):89–95, 1971.
- P. Goldreich and J. Kwan. Astrophysical masers. V. pump mechanisms for H_2O masers. *The Astrophysical Journal*, 191:93–100, July 1974.
- F. Gounand et al. Superradiant cascading effects in rubidium Rydberg levels. *Journal of Physics B: Atomic and Molecular Physics*, 12(4):547, 1979.
- M. Gross et al. Maser oscillation and microwave superradiance in small systems of Rydberg atoms. *Physical Review Letters*, 43(5):343, 1979.
- M. Gross and S. Haroche. Superradiance: An essay on the theory of collective spontaneous emission. *Physics Reports*, 93:301–396, December 1982.
- S. Haroche et al. Time-resolved laser spectroscopy: quantum beats and superradiance, M. Prior and H. Shugart, eds. In *Proceedings of the Fifth International Conference. July 26-30, 1976, Berkeley, California, U.S.A.*, page 179, New York: Plenum Press, 1977.
- G. H. Hilmarsson. Fast radio bursts: an overview and follow-up observations (Master’s thesis). University of Iceland, 2015.
- Y. Kaluzny et al. Observation of self-induced Rabi oscillations in two-level atoms excited inside a resonant cavity: The ringing regime of superradiance. *Physical Review Letters*, 51(13):1175, 1983.
- J. I. Katz. Coherent emission in fast radio bursts. *Physical Review D*, 89:103009, May 2014.
- J. I. Katz. Inferences from the distributions of fast radio burst pulse widths, dispersion measures and fluences. *The Astrophysical Journal*, 818:19, February 2016.
- E. F. Keane et al. A fast radio burst host galaxy. *Nature*, 530:453–456, February 2016.

- H. R. Klöckner and W. A. Baan. The Treasure Chamber of the OH Megamaser Mrk 273. In *Proceedings of the 6th European VLBI Network Symposium. June 25-28 2002, Bonn, Germany*, page 175, 2002.
- A. Koekemoer et al. A water-vapour giga-maser in the active galaxy TXFS2226–184. *Nature*, 378:697–699, December 1995.
- N. D. Kylafis and K. G. Pavlakis. OH megamaser pumping models. *Highlights of Astronomy*, 11B:946–948, 1998.
- V. D. Laptev et al. Initial stage of a superradiance pulse in the case of delayed or prolonged excitation of matter. *Soviet Journal of Quantum Electronics*, 14(8):1105, 1984.
- K. Y. Lo. Mega-masers and galaxies. *Annual Review of Astronomy and Astrophysics*, 43:625–676, 2005.
- C. J. Lonsdale. OH megamasers, V. Mineese and M. Reid, eds. In *Cosmic Masers: From Proto-Stars to Black Holes, IAU Symposium, Astronomical Society of the Pacific, Volume 206. March 5-10, 2001, Angra dos Reis, Rio de Janeiro, Brazil*, page 413, 2002.
- D. Lorimer et al. A bright millisecond radio burst of extragalactic origin. *Science*, 318(5851):777–780, November 2007.
- J. Luan and P. Goldreich. Physical constraints on fast radio bursts. *The Astrophysics Journal Letters*, 785:L26, April 2014.
- M. Lyutikov et al. Fast radio bursts as giant pulses from young rapidly rotating pulsars. *Royal Astronomical Society*, 462(1):941–950, October 2016.
- J. C. MacGillivray and M. S. Feld. Limits of superradiance as a process for achieving short pulses of high energy. *Physical Review A*, 23(3):1334, March 1981.
- J. C. MacGillivray and M. S. Feld. Superradiance in experimentally relevant regimes, C. M. Bowden et al., eds. *Cooperative Effects in Matter and Radiation*, New York: Plenum Press, 1977.

- J. J. Maki et al. Influence of collisional dephasing processes on superfluorescence. *Physical Review A*, 40(9):5135, 1989.
- M. S. Malcuit et al. Transition from superfluorescence to amplified spontaneous emission. *Physical Review Letters* 59(11):1189, 1987.
- B. Marcote et al. The repeating fast radio burst FRB 121102 as seen on milliarcsecond angular scales. *The Astrophysical Journal Letters*, 834(2):L8, January 2017.
- K. Masui et al. Dense magnetized plasma associated with a fast radio burst. *Nature*, 528:523–525, December 2015.
- R. Narayan. The physics of pulsar scintillation. *Philosophical Transactions: Physical Sciences and Engineering*, 341(1660):151–165, October 1992.
- M. R. Pestalozzi et al. A general catalogue of 6.7-GHz methanol masers. *Astronomy & Astrophysics*, 432:737–742, 2005.
- E. Petroff et al. A real-time fast radio burst: polarization detection and multiwavelength follow-up. *Royal Astronomical Society*, 447(1):246–255, January 2015.
- E. Petroff et al. FRBCAT: The Fast Radio Burst Catalogue. *Publications of the Astronomical Society of Australia*, 33:e045, 2016.
- J. M. Raimond et al. Statistics of millimeter-wave photons emitted by a Rydberg-atom maser: an experimental study of fluctuations in single-mode superradiance. *Physical Review Letters*, 49(26):1924, 1982.
- F. Rajabi and M. Houde. Dicke’s superradiance in astrophysics. I – the 21 cm Line. *The Astrophysical Journal*, 826(2):216, 2016a.
- F. Rajabi and M. Houde. Dicke’s superradiance in astrophysics. II – the OH 1612 MHz line. *The Astrophysical Journal*, 828(1):57, 2016b.
- F. Rajabi and M. Houde. Explaining recurring maser flares in the ISM through large-scale entangled quantum mechanical states. *Science Advances*, 3:e1601858, March 2017.

- A. Rane et al. A search for rotating radio transients and fast radio bursts in the Parkes high-latitude pulsar survey. *Royal Astronomical Society*, 455(2):2207–2215, January 2016.
- V. Ravi et al. A fast radio burst in the direction of the Carina dwarf spheroidal galaxy. *The Astrophysical Journal Letters*, 799(1):L5, January 2015.
- V. Ravi et al. The magnetic field and turbulence of the cosmic web measured using a brilliant fast radio burst. *Science*, 354(6317):1249, December 2016.
- P. Scholz et al. The repeating fast radio burst FRB 121102: multi-wavelength observations and additional bursts. *The Astrophysical Journal*, 833(2):177, December 2016.
- N. Skribanowitz et al. Observation of Dicke superradiance in optically pumped HF gas. *Physical Review Letters*, 30(8):309, 1973.
- V. I. Slysh. Resonance stark effect in OH and H₂O interstellar masers. *Astrophysical Letters*, 14:213–216, 1973.
- L. G. Spitler et al. A repeating fast radio burst. *Nature*, 531:202–205, March 2016.
- A. A. Svidzinsky et al. Quantum amplification by superradiant emission of radiation. *Physical Review X*, 3(4):041001, October 2013.
- D. Thornton et al. A population of fast radio bursts at cosmological distances. *Science*, 341(6141):53–56, July 2013.
- H. J. van Langevelde et al. Anomalously excited OH and competition between maser transitions toward Centaurus A. *The Astrophysical Journal*, 448:L123-L126, August 1995.
- Q. H. F. Vrehen et al. Quantum beats in superfluorescence in atomic cesium. *Physical Review Letters*, 38(14):764, 1977.
- J. M. Weisberg et al. Discovery of pulsed OH maser emission stimulated by a pulsar. *Science*, 309(5731):106–110, July 2015.
- P. Zinoviev et al. Optical superradiance in mixed molecular crystals. *Laser Physics*, 1(1):1–21, 1991.

Python Code

```
1  #*****
   Superradiance code employing a 4th order Runge-Kutta method:
   forward z, forward t. This is similar to the method of
   lines and only valid if no backward propagating waves are
   considered. This code uses the slowly varying envelope
   approximation for the electric dipole case when focusing on
   the 1720 MHz transition in OH and all parameters are in SI
   units and variables are scaled as per:  $E' = (d \cdot TR / \hbar) E$ ,  $N' = (V/N) N$ ,  $P' = (V/Nd) P$ ,  $t' = t/TR$ ,  $z' = z$ .
2  #*****
3
4  import matplotlib #no display environment on SHARCNET so need
   to import
5  matplotlib.use('pdf') #must also comment out plt.show() in
   SHARCNET
6  import os #this line and the two above are used so compatible
   with SHARCNET
7  matplotlib.use('pdf')
8  from random import random, randint, uniform
9  import matplotlib.pyplot as plt
10 from pylab import *
11 import numpy as np
12 from tqdm import tqdm
```

```

13
14 #constants & parameters
15 omega = 2.*np.pi*(1720.5299*(10.**(-6.)))
16 eps = 8.85*10.**(-12.)
17 c = 3.*(10.**8.)
18 k0 = omega/c
19 hbar = (6.626*10.**(-34.))/(2.*np.pi)
20 n_mean = (10.**(-5.)) #mean inverted population density (in
    molecules/m^3)
21 lambdaOH = c/(1720.5299*(10.**(-6.))) #wavelength
22 T_1_ = 9.349*(10.**(-12.))# = gamma
23 Tsp = 1./T_1_
24 TR_mean = 1.0*(10.**(-6.))#mean superradiance characteristic
    time
25 L_mean = (Tsp/TR_mean)*(8.*np.pi)/(3.*n_mean*(lambdaOH**2.))
26 radius_mean = np.sqrt(lambdaOH*L_mean/np.pi)
27 A_mean = np.pi*(radius_mean**2.)
28 phi_diffraction_mean = (lambdaOH**2.)/A_mean # (15) from Dicke
    superradiance II paper (Rajabi & Houde, 2016)
29 V_mean = (np.pi*(radius_mean**2.))*L_mean
30 NN_mean = n_mean*V_mean #total inverted population
31 d = (3.*eps*c*hbar*(lambdaOH**2.)*T_1_/(4.*np.pi*omega))**0.5
    #dipole transition element
32 Lp = 1. #scaling of z-axis
33 #z-space

```

```

34 Ngridz = 1000 #number of steps in z-axis
35 zmax = (L_mean/Lp)
36 dz = zmax/Ngridz
37 z = np.linspace(0.0,zmax,Ngridz+1)
38 #time
39 Ngridt = 1000 #number of steps in t-axis; should be larger than
    tmax (i.e. tmax/TR if tmax in SI units)
40 tmax = 1000. #time limit; is actually tmax*TR_mean in SI units
    (re-scaled later in code)
41 dt = tmax/Ngridt #this should be less than or equal to TR
42 t = np.linspace(0.0,tmax,Ngridt+1) #this is tau/TR; len(t) =
    interval
43
44 #arrays storing values for each single realization
45 Ep = np.zeros(((Ngridz+1),len(t)),dtype=np.complex_) #number of
    rows = len(z)
46 Pp = np.zeros(((Ngridz+1),len(t)),dtype=np.complex_)
47 N = np.zeros(((Ngridz+1),len(t)),dtype=np.complex_) #using np.
    complex_ or complex seems to work; check higher precision
    arithmetic packages
48
49 #array storing values for different realizations by summing
    from all realizations
50 #since the t-axis is scaled by TR_mean for all realizations,
    they can be added together in time

```

```

51 #although if L is changing, then only intensities at end of
    sample for each realization should be added
52 IntensitySUM = np.zeros(((Ngridz+1),len(t)),dtype=np.complex_)
53
54 T_time_scale = 0.5 #uncommenting this line and lines 73-75 and
    lines 79-80
55 #allows for arbitrary "additional pump(s)" that can be
    arbitrarily added
56 #to arrive and restore N and P as in lines 73-75 and lines
    79-80, respectively
57 def dN(N,P,E,k,i,kN,kP,kE,TR,T1):
58     kNN = ((1j)*((P[k,i]+kP)*(E[k,i]) - np.conj(E[k,i])*np.conj
        (P[k,i]+kP)) \
59         - (N[k,i]+kN)/(T1/TR_mean)) #this must be TR_mean if
        constant time-axis used
60 #     if (i >= int(0.2*Ngridt)) and (i <= int(0.21*Ngridt)):
61 #     if i == int(T_time_scale*Ngridt):
62 #         kNN = 0.7*(0.5*np.cos(theta0) - N[k,i])
63     return kNN
64 def dP(N,P,E,k,i,kN,kP,kE,TR,T2):
65     kPP = ((2j)*(np.conj(E[k,i]))*(N[k,i]+kN) - (P[k,i]+kP)/(T2
        /TR_mean)) #this must be TR_mean if constant time-axis
        used
66 #     if (i >= int(0.2*Ngridt)) and (i <= int(0.21*Ngridt)):
67 #     if i == int(T_time_scalen(theta0) - P[k,i])

```

```

68     return kPP
69 def dE(N,P,E,k,i,kN,kP,kE,constant3,Ldiff,Lp):
70     kEE = ((1j*constant3)*np.conj(P[k,i]) - (E[k,i]+kE)/(Ldiff/
71         Lp))
72     return kEE
73 #used to hold values for different realizations for plotting at
74     end of code, if desired
75
76 TR_list = []
77
78 cycle_STOP = 100 #number of cycles/superradiant realizations
79
80 #this provides a progress bar but only updates per cycle
81 #i.e. if only doing one cycle, will not see progress update
82 #although can manually change this easily so that it updates
83     per gridstep
84
85 progress = tqdm(total=100.)
86 total = 100.
87 progress_cycles = (total)/(cycle_STOP)
88
89 #these arrays store values strictly at z = L
90 TOTAL_E = np.zeros((cycle_STOP+1,len(t)),dtype=np.complex_)
91 TOTAL_I = np.zeros((cycle_STOP+1,len(t)))
92 TOTAL_N = np.zeros((cycle_STOP+1,len(t)),dtype=np.complex_)
93 TOTAL_P = np.zeros((cycle_STOP+1,len(t)),dtype=np.complex_)

```

```

90
91 cycles = 0
92 while cycles < cycle_STOP:
93     mu1 = TR_mean
94     sigma1 = 0.0000000001*mu1 #standard deviation of T_R
95     TR = np.random.normal(mu1, sigma1) #Gaussian distributed TR
96     TR_list.append(TR)
97     T1 = 10000.*(10.**(-6.)) #relaxation time - SI units
98     T2 = 10000.*(10.**(-6.)) #dephasing time - SI units
99     n_actual = (Tsp/TR)*(8.*np.pi)/(3.*L_mean*(lambdaOH**2.)) #
        assuming constant length although can remove
100 #this assumption my using different value for "L_mean"
101 NN = n_actual*V_mean #total inverted population for this
        realization
102 Fn = 1. # = (radius**2.)/(lambdaOH*L)
103 Ldiff = Fn*L_mean/0.35
104 constant3 = (omega*TR_mean*NN*(d**2.))*Lp/(2.*c*hbar*eps*
        V_mean) #the TR_mean has to be the outside one
105 #since it is used for scaling of t-axis; only NN varies
        here
106
107 theta0 = 2./np.sqrt(NN)
108 TD = 0.25*(np.log(theta0/(2.*np.pi)))*2.*TR
109 T0 = np.log(theta0/2.) #pg.30 Benedict et al. discuss area
        of initial pulse

```



```

110     if cycle_STOP == 1:
111         cycles = cycles + 1
112     progress.update(progress_cycles)
113     k = 0
114     while k < (len(z) - 1):
115
116     #-----calculating NE, PpE, and EpE-----
117
118         hz = z[k+1]-z[k] #hz is positive
119         #this simply makes entries for arrays all zeros again
120         EpM = Ep
121         PpM = Pp
122         NM = N
123
124         theta0_mean = 2./np.sqrt(NN) #initial Bloch angle = 2/
125             np.sqrt(NN)
126         sigma_theta0 = 0.0001*theta0_mean
127         SIGMA_T0 = int(sigma_theta0/theta0_mean) #Gaussian
128             distributed theta0
129         theta0_k = (np.random.normal(theta0_mean, sigma_theta0)
130             )
131
132         i = 0
133         while i < (len(t) - 1):
134             ht = t[i+1] - t[i]

```

```

132
133     theta0_i = theta0_mean#np.abs(np.random.normal(
        theta0_mean, sigma_theta0))
134
135 #     Initial conditions
136     Pp[k,0] = 0.5*np.sin(theta0_k)#np.sin(z[:]/(0.001*
        Lp))#(np.e**((-z[:])**2.)/(0.001*L_mean)**2.))
137     N[k,0] = 0.5*np.cos(theta0_k)#the above lines
        commented out is just one way to alter initial
        conditions
138     if i == 0:
139         EpM[k,0] = 0.
140 #     Boundary conditions
141     EpM[0,i] = 0. #E boundary condition
142     if k == 0:
143         PpM[0,i] = 0.5*np.sin(theta0_i)*(np.e**(-t[i]*
            TR_mean/T2))
144         NM[0,i] = 0.5*np.cos(theta0_i)*(np.e**(-t[i]*
            TR_mean/T1))
145
146 #     4th-order Runge-Kutta
147 #     in time
148     kEb1 = dE(NM,PpM,EpM,k,i,0.,0.,0.,constant3,Ldiff,
        Lp)
149     kEb2 = dE(NM,PpM,EpM,k,i,0.,0.,0.5*hz*kEb1,

```

```

constant3,Ldiff,Lp)
150 kEb3 = dE(NM,PpM,EpM,k,i,0.,0.,0.5*hz*kEb2,
      constant3,Ldiff,Lp)
151 kEb4 = dE(NM,PpM,EpM,k,i,0.,0.,hz*kEb3,constant3,
      Ldiff,Lp)
152 # in z
153 kNb1 = dN(NM,PpM,EpM,k,i,0.,0.,0.,TR,T1)
154 kPb1 = dP(NM,PpM,EpM,k,i,0.,0.,0.,TR,T2)
155 kNb2 = dN(NM,PpM,EpM,k,i,0.5*ht*kNb1,0.5*ht*kPb1
      ,0.,TR,T1)
156 kPb2 = dP(NM,PpM,EpM,k,i,0.5*ht*kNb1,0.5*ht*kPb1
      ,0.,TR,T2)
157 kNb3 = dN(NM,PpM,EpM,k,i,0.5*ht*kNb2,0.5*ht*kPb2
      ,0.,TR,T1)
158 kPb3 = dP(NM,PpM,EpM,k,i,0.5*ht*kNb2,0.5*ht*kPb2
      ,0.,TR,T2)
159 kNb4 = dN(NM,PpM,EpM,k,i,ht*kNb3,ht*kPb3,0.,TR,T1)
160 kPb4 = dP(NM,PpM,EpM,k,i,ht*kNb3,ht*kPb3,0.,TR,T2)
161
162 EpM[k+1,i] = EpM[k,i] + (hz/6.)*(kEb1 + 2.*kEb2 +
      2.*kEb3 + kEb4)
163 NM[k,i+1] = NM[k,i] + (ht/6.)*(kNb1 + 2.*kNb2 + 2.*
      kNb3 + kNb4)
164 PpM[k,i+1] = PpM[k,i] + (ht/6.)*(kPb1 + 2.*kPb2 +
      2.*kPb3 + kPb4)

```

```

165
166 #         Initial conditions
167         Pp[k,0] = 0.5*np.sin(theta0_k)#np.sin(z[:] / (0.001*
            Lp))#(np.e**((-z[:])**2.) / (0.001*L_mean)**2.))
168         N[k,0] = 0.5*np.cos(theta0_k)#the above lines
            commented out is just one way to alter initial
            conditions
169         if i == 0:
170             EpM[k,0] = 0.
171 #         Boundary conditions
172         EpM[0,i] = 0. #E boundary condition
173         if k == 0:
174             PpM[0,i] = 0.5*np.sin(theta0_i)*(np.e**(-t[i]*
                TR_mean/T2))
175             NM[0,i] = 0.5*np.cos(theta0_i)*(np.e**(-t[i]*
                TR_mean/T1))
176
177         i = i + 1
178     k = k + 1
179
180     if k == (len(z)-1): #this is only because i dont have
        extra iteration for N and P in z
181         if i == (len(t)-1): #and this smooths N, P, and E
            at grid boundaries
182             EpM[:,i] = EpM[:,i-1] #for E at at end of time

```

```

183         NM[k,:] = NM[k-1,:] #for N and P at end of
           sample
184         PpM[k,:] = PpM[k-1,:] #i.e. at end of z-axis
185
186     #index for the below arrays corresponds to which
           superradiant sample it is (i.e. which cycle)
187     #and only stores the values at the end of the sample
188         Ep_FINAL = ((EpM[int(Ngridz-1.),:])/(d*TR_mean/
           hbar)) #the electric field is in SI units
189         I_SR = ((0.5*c*eps*((Ep_FINAL*np.conj(Ep_FINAL)
           ))).real) # = Itot
190         TOTAL_E[cycles] = Ep_FINAL
191         TOTAL_I[cycles] = I_SR
192         TOTAL_N[cycles] = NM[int(Ngridz-1.),:] #still
           scaled by N/V
193         TOTAL_P[cycles] = PpM[int(Ngridz-1.),:] #still
           scaled by d*N/V
194         IntensitySUM = IntensitySUM + ((0.5*c*eps*(((
           EpM/(d*TR_mean/hbar))*np.conj((EpM/(d*
           TR_mean/hbar)))))).real)
195
196     #could technically start a second loop, and even more, to
           continue
197     #finding solution inside the boundary of the grid to ensure
           an

```

```

198     #"stable" solution is reached; unless pathological boundary
        /initial conditions are applied
199     #all solutions should be stable (as observed when tested);
        increasing the number of grid points is analogous
200     #although this alternative would allow for E to have an
        updated dependence on N and P
201     #as they vary in z, too, since this is missing in its RK4
        step
202     cycles = cycles + 1
203 progress.close()
204
205 I_nc = NN_mean*hbar*omega*(1./(A_mean*Tsp))*(
        phi_diffraction_mean/(4.*np.pi))
206 #the above and below lines should be equivalent expressions
207 I_nc = (2./3.)*hbar*omega/(A_mean*TR_mean) #should technically
        be multiplied by "cycles" since there are that many
        superradiant samples
208 IntensityRatio = IntensitySUM.real/(NN_mean*I_nc) #summed
        intensity for all z scaled by N*I_nc
209
210 newpath = r'OH_1720MHz_SVEA_superradiance_theta0_sigma='+str(
        SIGMA_T0)+'_TR='+str(TR_mean)+'_n='+str(n_mean)+'_tmax=TR*'+
        str(tmax)+'_T1='+str(T1)+'_T2='+str(T2)+'_L='+str(L_mean)+'
        _zmax='+str(zmax)+'_Ngridz='+str(Ngridz)+'_Ngridt='+str(
        Ngridt)+'_cycles='+str(cycles)+'_T_time_scale='+str(

```

```

    T_time_scale)
211 if not os.path.exists(newpath):
212     os.makedirs(newpath)
213
214 z = z*Lp #ensures the axis scales are in SI units
215 t = t*TR_mean
216
217 j = 0
218 IntensityFINAL = np.zeros(len(t))
219 while j < len(TOTAL_I[:,0]):
220     IntensityFINAL += TOTAL_I[j,:]
221     j = j + 1
222 #IntensityRatio = ((0.5*c*eps*((E_SR*np.conj(E_SR)))).real)#
    TOTAL_E
223
224 t = TR_mean*np.linspace(0.0,tmax,Ngridt+1)
225
226 plt.figure(1)
227 #histogram of TR for different realizations
228 n, bins, patches = plt.hist(TR_list, 50, normed=1, facecolor='
    green', alpha=0.75)
229 # add a 'best fit' line
230 y = mlab.normpdf( bins, mu1, sigma1)
231 plt.xlabel(r"$ \tau (s) $")
232 plt.ylabel('Relative Frequency of T_R (not normalized)')

```

```

233 plt.ticklabel_format(style='sci', axis='x', scilimits=(0,0))
234 l = plt.plot(bins, y, 'r--', linewidth=1)
235 plt.savefig(str(newpath)+'Histogram_TR.pdf')
236 #plt.show()
237
238 plt.figure(2)
239 fig, ax = plt.subplots(figsize=(20, 20))
240 plt.subplot(221)
241 plt.plot(t, IntensityRatio[0,:], 'k:', linewidth = 1.5)
242 plt.ylabel(r"$ \frac {I_{SR}}{NI_{nc}} $" )
243 plt.subplot(222)
244 plt.plot(t, IntensityRatio[int(0.33*len(z)) :], 'k:', linewidth =
    1.5)
245 plt.subplot(223)
246 plt.plot(t, IntensityRatio[int(0.66*len(z)) :], 'k:', linewidth =
    1.5)
247 plt.subplot(224)
248 plt.plot(t, IntensityRatio[len(z)-1,:], 'k:', linewidth = 1.5)
249 plt.xlabel(r"$ \tau (s) $" )
250 plt.savefig(str(newpath)+'I_vs_t.pdf')
251 #plt.show()
252
253 plt.figure(3)
254 fig, ax = plt.subplots(figsize=(20, 20))
255 plt.subplot(221)

```



```

256 plt.plot(z,IntensityRatio[:,0], 'k:',linewidth = 1.5)
257 plt.ylabel(r"$ \frac {I_{\text{SR}}}{NI_{\text{nc}}}$")
258 plt.subplot(222)
259 plt.plot(z,IntensityRatio[:,int(0.33*len(t))], 'k:',linewidth =
    1.5)
260 plt.subplot(223)
261 plt.plot(z,IntensityRatio[:,int(0.66*len(t))], 'k:',linewidth =
    1.5)
262 plt.subplot(224)
263 plt.plot(z,IntensityRatio[:,len(t)-1], 'k:',linewidth = 1.5)
264 plt.xlabel('z (m)')
265 plt.savefig(str(newpath)+'/I_vs_z.pdf')
266 #plt.show()

```